Title
Dynamics of energetic particle driven modes and MHD modes in wall-stabilized high-β plasmas on JT-60U and DIII-D

Journal
Nuclear Fusion, 53(12)

ISSN
0029-5515

Authors
Matsunaga, G
Okabayashi, M
Aiba, N
et al.

Publication Date
2013-12-01

DOI
10.1088/0029-5515/53/12/123022

Nucl. Fusion **53** (2013) 123022 (13pp) doi:10.1088/0029-5515/53/12/123022

Dynamics of energetic particle driven modes and MHD modes in wall-stabilized high-β plasmas on JT-60U and DIII-D

G. Matsunaga[1], M. Okabayashi[2], N. Aiba[1], J.A. Boedo[3], J.R. Ferron[4], J.M. Hanson[5], G.Z. Hao[6], W.W. Heidbrink[7], C.T. Holcomb[8], Y. In[9], G.L. Jackson[4], Y.Q. Liu[10], T.C. Luce[4], G.R. McKee[11], T.H. Osborne[4], D.C. Pace[4], K. Shinohara[1], P.B. Snyder[4], W.M. Solomon[2], E.J. Strait[4], A.D. Turnbull[4], M.A. Van Zeeland[4], J.G. Watkins[12], L. Zeng[13], the DIII-D Team and the JT-60 Team

[1] Japan Atomic Energy Agency, Naka, Japan
[2] Princeton Plasma Physics Laboratory, Princeton, NJ, USA
[3] Department of Aerospace and Mechanical Engineering, University of California, San Diego, CA, USA
[4] General Atomics, San Diego, CA, USA
[5] Department of Applied Physics and Applied Mathematics, Columbia University, New York, NY, USA
[6] Southwestern Institute of Physics, Chengdu, People's Republic of China
[7] Department of Physics and Astronomy, University of California, Irvine, CA, USA
[8] Lawrence Livermore National Laboratory, Livermore, CA, USA
[9] FAR-TECH, Inc., 10350 Science Center Dr, Suite 150, San Diego, CA, USA
[10] Euratom/CCFE Fusion Association, Culham Science Centre, Abingdon, UK
[11] Department of Engineering Physics, University of Wisconsin at Madison, Madison, WI, USA
[12] Sandia National Laboratories, Albuquerque, NM, USA
[13] Department of Electrical Engineering and Plasma Science and Technology Institute, University of California, Los Angeles, CA, USA

Received 5 March 2013, accepted for publication 4 November 2013
Published 25 November 2013
Online at stacks.iop.org/NF/53/123022

Abstract
In the wall-stabilized high-β plasmas in JT-60U and DIII-D, interactions between energetic particle (EP) driven modes (EPdMs) and edge localized modes (ELMs) have been observed. The interaction between the EPdM and ELM are reproducibly observed. Many EP diagnostics indicate a strong correlation between the distorted waveform of the EPdM and the EP transport to the edge. The waveform distortion is composed of higher harmonics ($n \geqslant 2$) and looks like a density snake near the plasma edge. According to statistical analyses, ELM triggering by the EPdMs requires a finite level of waveform distortion and pedestal recovery. ELM pacing by the EPdMs occurs when the repetition frequency of the EPdMs is higher than the natural ELM frequency. EPs transported by EPdMs are thought to contribute to change the edge stability.

(Some figures may appear in colour only in the online journal)

1. Introduction

For a fusion reactor, high-β operation is advantageous to achieve higher fusion output power, because the fusion output is proportional to the square of β [1]. In principle, the high-β regime between the no-wall and ideal-wall MHD limits is achievable with a conducting wall close to the plasma to stabilize ideal kink-ballooning modes that limit the β-value [2]. Therefore, this regime can be called the 'wall-stabilized high-β regime'. This high-β regime has been well investigated, but not fully understood. In particular, a resistive wall mode (RWM) must also be suppressed or controlled because the RWM also limits the achievable β-value [2]. Especially for high-β burning plasmas, energetic particle (EP) contributions to

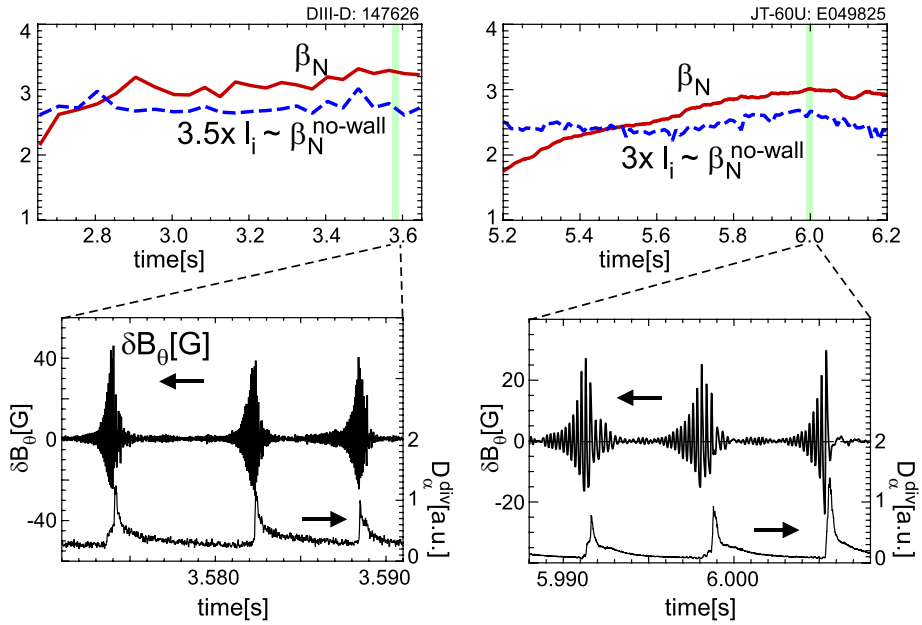

Figure 1. High-β_N discharges on (left) DIII-D and (right) JT-60U where ELM triggering by EPdMs is observed: (top) normalized β with no-wall β limits, (bottom) expanded waveforms of Mirnov and D_α signals.

MHD stability may be important. Also, interactions between energetic-particle-driven modes (EPdMs) and MHD modes with marginal stability are possible due to a significant EP density in burning plasmas. An impact of EPdMs on the RWM has been reported in JT-60U and DIII-D. It has been reported that EPdMs can induce RWM onset [5, 6]. Moreover, in high-β operation on JT-60U, interaction between the EPdM and energy localized modes (ELMs), thus ELM triggering by the EPdM, has been observed [3]. Moreover, this ELM triggering behaves like the so-called 'ELM mitigation' on JT-60U, where the ELM energy loss decreases and the ELM frequency increases [4]. Recently, ELM triggering by the EPdM has been also observed on DIII-D. These observations in both devices imply a new common MHD physics in high-β plasmas suggesting that the EP contribution is important even for edge stability in high-β burning plasmas.

In this paper, we report on ELM triggering by EPdMs based on experimental observations and MHD stability analyses for JT-60U and DIII-D. In section 2, examples of ELM triggering by the EPdM and its EP transport are described. In particular, one of the distinct features of the EPdM, waveform distortion, that strongly correlates with EP transport, is mentioned. In section 3, some necessary conditions for ELM triggering and pacing are discussed. In section 4, possible mechanisms of this phenomenon are discussed.

2. Observation of ELM triggering by EPdMs

ELM triggering by EPdMs has been observed in JT-60U and DIII-D wall-stabilized high-β plasmas. Figure 1 indicates typical observations with toroidal magnetic field and plasma current values of $B_t/I_p = 1.7\,\mathrm{T}/1.0\,\mathrm{MA}$ on DIII-D and $B_t/I_p = 1.5\,\mathrm{T}/0.9\,\mathrm{MA}$ on JT-60U. The top panels indicate normalized β-values defined as $\beta_N \equiv \beta/(I_p/aB_t)$ (%Tm/MA) and roughly estimated no-wall β limits described as $3.5\,l_i$ on DIII-D and $3.0\,l_i$ on JT-60U by using the internal inductance l_i. The bottom figures in figure 1 show the expanded waveforms of Mirnov signals and D_α emissions. The EPdM fishbone-like bursts appeared when β_N exceeded the no-wall β_N limit. The EPdMs are called 'energetic particle driven wall modes (EWMs)' on JT-60U emphasizing the role of wall stabilization [5] and 'off-axis fishbone modes (OFMs)' on DIII-D emphasizing the similarity to classical fishbones [6]. Hereafter, in this paper, EPdMs is used for both modes. Note that these modes are usually observed in discharges with a large fraction of EP, thus, $\beta_{EP}/\beta_{total} \geqslant 25\%$, where β_{EP} and β_{total} are β-values estimated using the EP and total pressures. These observations show that ELMs are clearly triggered by the EPdMs. Figure 2 shows typical pedestal behaviour during EPdMs for DIII-D and JT-60U. From the top, time evolutions of ion temperatures around the pedestal region measured by charge exchange recombination spectroscopy systems (T_i), Mirnov signals, and D_α emissions are shown. There are four EPdMs in each panel. The second and fourth EPdMs in the DIII-D case and the fourth EPdM in the JT-60U case are not accompanied by ELM triggering. The EPdMs with ELM triggering are always observed together with pedestal crashes. This indicates that the D_α spikes synchronized with the EPdMs are due to the pedestal crashes in a similar way to natural ELMs.

Both observations imply that common MHD physics exists and that the EP contribution becomes important even for edge stability in high-β burning plasmas. Note that ELM triggering by the EPdM on DIII-D is observed only with off-axis neutral beams (NBs) [8]. It is thought that EPs injected from the off-axis NBs are effective for driving the EPdM and then, ELM triggering by the EPdM was clearly observed.

2.1. EPdM to trigger ELM and its EP transport

The Mirnov signals of the EPdMs that trigger an ELM as observed on DIII-D and JT-60U are shown in figure 3. The

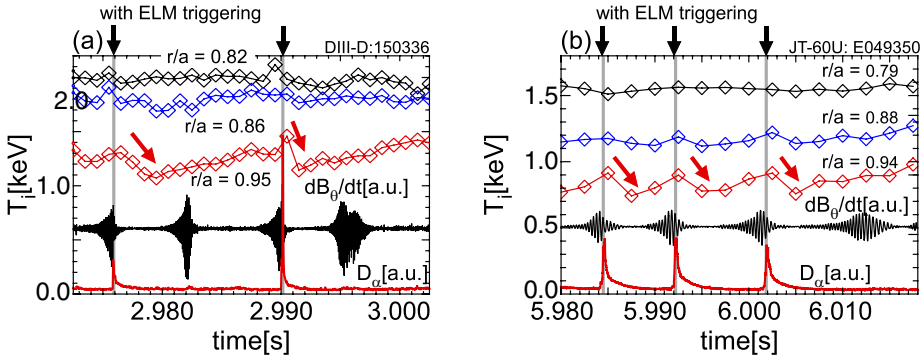

Figure 2. Pedestal crashes with ELM triggering by EPdM for typical (*a*) DIII-D and (*b*) JT-60U cases. Curves with symbols are time evolutions of ion temperatures around the pedestal region measured by charge exchange recombination spectroscopy, Mirnov signals, and D_α emissions. Grey lines indicate ELMs triggered by EPdMs.

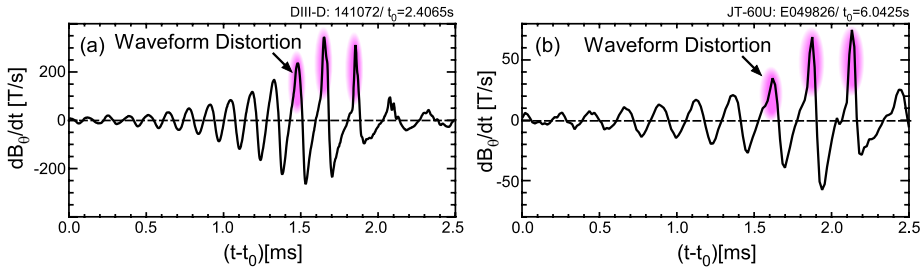

Figure 3. Expanded Mirnov signals of EPdMs observed on (*a*) DIII-D and (*b*) JT-60U. Highlighted regions are waveform distortions.

main characteristics commonly found on JT-60U and DIII-D are as follows [3, 7, 9]:

- Initial mode frequencies are close to the precession frequency of trapped EPs injected by NBs, i.e. around 3 kHz on JT-60U and 15 kHz on DIII-D,
- Toroidally (fundamentally) $n = 1$ mode structure,
- Poloidal magnetic structure measured at the wall is $m \sim 3$ and the amplitude at the low field side is larger than that at the high field side (ballooning structure),
- Radially global structure with a maximum amplitude around the $q = 2$ surface,
- Mode frequency is chirping down as the mode amplitude increases,
- Doppler-shifted mode frequency,
- Triggering RWM onset despite sufficient plasma rotation for RWM stabilization,
- Appearance above the no-wall β_N-limit,
- Enhancement of EP transport to the edge region, and
- Strong waveform distortion of magnetic and density fluctuations and EP diagnostic signals (non-sinusoidal oscillation).

We have observed intense EP transport and loss by the EPdM on DIII-D [9]. These were first found on DIII-D by the extensive EP diagnostics. Namely, the plastic scintillator for neutron yield [10], the fast ion loss detector (FILD) [11], beam emission spectroscopy (BES) diagnostic measuring fast ion D_α (FIDA) light [12], dedicated filter-based FIDA diagnostic [13], and the neutral particle analyser (NPA) [14] are utilized. Note that ion transport was observed on JT-60U. However, it could not be determined whether it was thermal ions or EPs due to a lack of EP diagnostics [4]. Figure 4 illustrates EP signals measured by these diagnostics. As seen in the figure, these signals usually look like intense spikes synchronized with the waveform distortion on Mirnov signal. This is the same as the so-called beacon seen with fishbones on PDX [15]. Namely, the toroidal location where the EP transport is enhanced is toroidally rotating with growing amplitude (i.e. six times in these panels). Moreover, the toroidal width where the EP transport is enhanced is about 60° as estimated from time evolutions of the signals such as BES, FIDA and NPA. Note that the FILD signal indicates a narrower extent than the others because the FILD signal tends to reflect a quite local behaviour, thus the FILD is sensitive to poloidal and toroidal locations, EP energy and pitch angle.

Figure 5(*a*) shows a camera image from the FILD located outside the plasma [16]. There are three EP loss regions during the EPdM event on DIII-D with $(E, v_\parallel/v) = (65\,\mathrm{keV}, 0.19)$, $(70\,\mathrm{keV}, 0.27)$ and $(81\,\mathrm{keV}, 0.51)$, where E and $v_\parallel/v$ are particle energy and pitch angle, respectively. The camera exposure time is 500 μs from $t = 1712.50$ ms and the scintillator decay time is 490 ns (~2 MHz bandwidth). The first two regions only appear on the camera frame acquired during the EPdM. The third region is actually NB prompt loss from the counter-injected beam. The loss orbit trajectory of the second region with $(E, v_\parallel/v) = (70\,\mathrm{keV}, 0.27)$ is shown in figure 5(*b*). The EPdM losses are clearly on trajectories that are pushed far out toward the plasma edge. The data indicate that the EPdM enhances the EP loss. From this, we have found that the EPdM can transport 'trapped EPs' to the edge and finally expel them outside the plasma.

The EPdM waveform appears to be an $n = 1$ sinusoidal oscillation with a small amplitude in the initial phase. However, the waveform deviates from $n = 1$ sinusoidal oscillation as the amplitude becomes larger, this is the 'waveform distortion' exhibited in figure 3. Namely, the

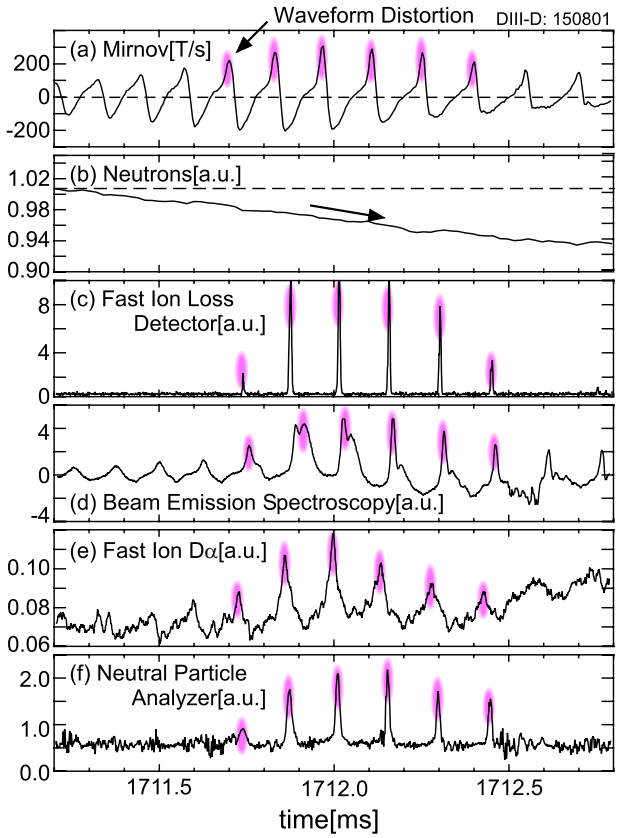

Figure 4. Signals measured by EP diagnostics: (*a*) Mirnov signal, (*b*) neutron yield by plastic scintillator, (*c*) fast ion loss detector (FILD), (*d*) beam emission spectroscopy (BES) diagnostic measuring fast ion D_α (FIDA) light, (*e*) dedicated filter-based FIDA diagnostic, and (*f*) neutral particle analyser (NPA). Highlighted regions correspond to waveform distortions on DIII-D.

Mirnov signal has an up-down asymmetry in the oscillation waveform. This waveform distortion of the EPdM is one of its distinct features [7, 9]. The waveform distortion seems to strongly correlate with the EP transport. To estimate the correlation between waveform distortion and EP transport, quantitatively, fundamental and distortion components must be defined. Figure 6 shows a Fourier spectrum of a Mirnov signal during the EPdM. In this paper, the fundamental and distortion components are defined as $n = 1$ and $n \neq 1$ components, respectively. These $n \neq 1$ components appear as higher harmonics in time with frequencies of $f = 2f_0, 3f_0, \ldots$ where f_0 is the EPdM fundamental frequency. In the real space, these correspond to higher toroidal mode number of $n = 2, 3$ and so on.

Figure 7 shows the relationship between the fundamental and distortion components and the EP transport to the edge. The EPdM is shown in figures 7(*a*) and (*b*) as an integrated Mirnov signal δB_θ and as envelopes $\delta B_\theta^{\rm env}$ of the decomposed fundamental (dotted) and distortion (solid) components. Note that the fundamental and distortion parts are decomposed by digital high/low pass filters with cut-off frequency f_c located between fundamental and second harmonic as shown in figure 6. An example of an EP density fluctuation at the edge measured by the BES system without diagnostic NBs is shown figure 7(*c*). When the NBs used for the BES measurement are off, the BES signals become passive fast ion D_α emissions (FIDA) [12]. Namely, the passive BES provides the EP density fluctuation $\tilde{n}_{\rm EP}$ at the edge region. Large spikes corresponding to intense increases of EP transport are synchronized with the Mirnov signals. The EP density increases as the distortion component increases. It should be noted that the EPdM in this figure is unaccompanied by ELM triggering. In figure 7(*d*), dotted and solid curves indicate relations of the EP density at edge region versus fundamental and distortion components, respectively. The EP behaviour at the edge strongly (and linearly) correlates with the distortion component rather than with the fundamental. Other EP diagnostics and floating potential $V_{\rm f}^{\rm SOL}$ in the SOL have similar dependences. From this, the distortion component is seen to increase EP transport to the edge region more rapidly than the fundamental component.

2.2. *Waveform distortion of EPdM*

The mode distortion discussed in the previous section 2.1 is commonly observable on various magnetic pickup probes. As discussed below, using the magnetic perturbations measured with the Mirnov toroidal array, we have demonstrated that the mode distortion is due to a spatially-distorted mode structure rather than by temporal variation in the rotation frequency, which could be due to a highly-toroidally-localized non-uniformity such as localized-magnetic perturbation or machine-hardware related singularity.

The mode structure in any toroidal location on the mid-plane can be characterized with a quasi-fixed phase velocity and higher $n \neq 1$ harmonics components. Figure 8(*a*) shows the magnetic perturbation observed by Mirnov probes located at nine different toroidal locations on the outboard side mid-plane. Here, signals were prepared by integrating in time the signals of Mirnov probes. Signals at all toroidal locations showed the fundamental $n = 1$ oscillation of frequency ~14 kHz. The mode propagated in the co-current direction with a semi-fixed phase velocity, judging from the time evolution in comparison with neighbouring signals.

The amplitude of individual harmonic components was nearly identical at different toroidal locations as shown in figure 8(*b*). The amplitude and phase of harmonics components were calculated analysing two periods of oscillatory behaviour with time period (t = 4862.50–4862.70 ms) in figure 8(*a*). The fundamental $n = 1$ amplitude was higher by a factor of 3–4 than that of other components ($n \neq 1$), however, the distortion components ($n \neq 1$) remained finite up to n = 4–5. The magnitude of 'mode distortion' used in the previous section is defined as the summation of the high $n > 1$ component amplitude. As shown here, the mode distortion ($n \neq 1$) amplitude, namely, the magnitude of each harmonic is independent from the choice of sensor location. It seems that no systematic variation exists between the fundamental $n = 1$ amplitude and other $n \neq 1$ amplitudes.

The phase of fundamental and distortion components are tightly coupled together forming an integrated rigid mode structure. Figure 8(*c*) shows the phase relation between the fundamental and distortion portion at various toroidal locations. It is obvious that no location behaves differently compared with other places. The toroidal phase

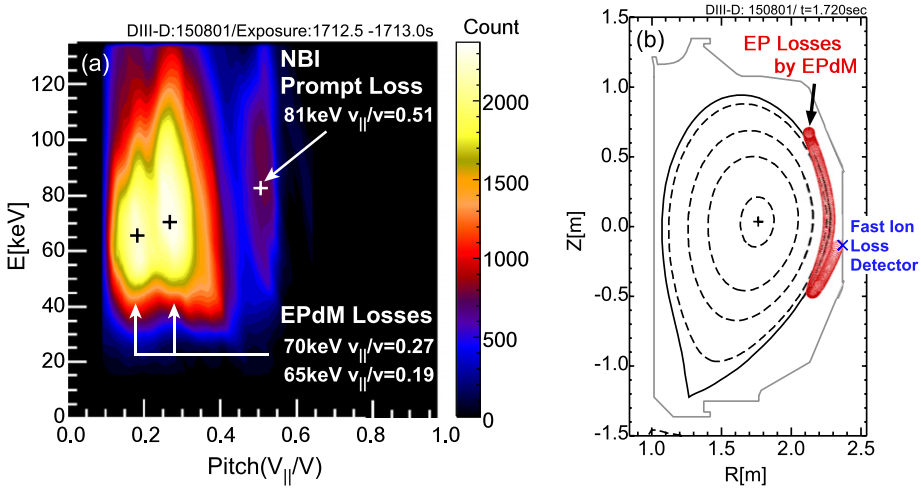

Figure 5. (*a*) Camera image from the FILD during EPdM on DIII-D and (*b*) calculated EP loss orbit.

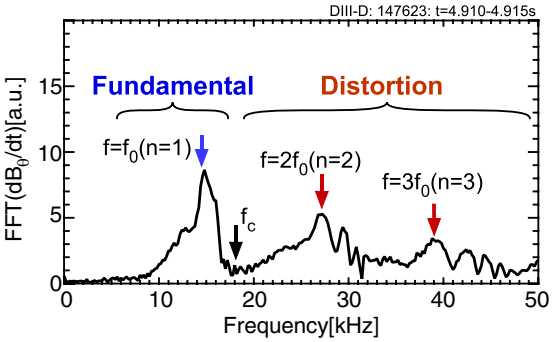

Figure 6. Fourier spectrum of the Mirnov signal during EPdM on DIII-D. f_c is the cut-off frequency for digital high/low pass filters to decompose the fundamental and distortion parts.

of fundamental $n = 1$ mode varies linearly against the probe location angle and, furthermore, the phase of $n \neq 1$ components has a linear dependence on the toroidal direction, the same as that of the fundamental. Thus, we conclude that analysis with a temporal distortion is equivalent to the analysis utilizing a spatial distortion. No ambiguity arises in discussing the spatial distortion with the approach discussed in section 2.1.

Fourier analysis of Mirnov signal during the EPdM indicates that the waveform distortion is composed of higher harmonics $f \geqslant 2f_0$ and higher toroidal mode number $n \geqslant 2$. Figure 9 shows a phase relation between the fundamental (dotted) and distortion (bold) components of the EPdM. In these polar plots, the azimuthal angle and radial direction correspond to the toroidal angle and amplitudes of the fundamental and distortion components respectively. The toroidal angle is calculated from one period in time where the mode is rigidly rotating in the toroidal direction. Note that since the snap-shot of the EPdM toroidal structure at a certain time remains distorted, the distortion is not a sinusoidal structure rotating with a modulated rotation velocity but the distorted structure rigidly rotating. Figure 9(*b*) shows that the peaks of both the fundamental and distortion components are well-aligned. Moreover, at 90° phase shift from the peak (in both directions), the distortion component still has finite amplitude. Therefore, the distortion has a global toroidal structure made up of low-$n > 1$ components, furthermore, these components are always excited in phase together, thus, they have maximum amplitude at the same toroidal phase relative to the fundamental. A possible mechanism of this distortion is the localized pressure increase as was observed in sawtooth-precursor induced high-n ballooning modes [17], where the ballooning structure appeared only in the region where the precursor fluctuation is at maximum amplitude. Another possibility is due to a different instability branch being excited by the shift of the EP distribution during the EPdM time evolution as discussed later.

Figures 10(*a*)–(*c*) show the experimentally obtained poloidal magnetic field of an EPdM and the decomposed fundamental and distortion components from DIII-D. The patterns are an integrated Mirnov signal, δB_θ, along with fundamental and distortion components as a function of poloidal location and time. Here, time evolution is equivalent to toroidal location because the mode is rigidly rotating in the toroidal direction. The poloidal pattern of δB_θ indicates that the mode pitch (the ratio between poloidal and toroidal components) is not uniform in the poloidal direction as shown indicated by the dotted lines. Note that the EPdM waveform from JT-60U exhibits similar distortion. Figures 10(*d*)–(*f*) show poloidal magnetic field perturbation patterns of unstable modes calculated with the MARS-F code [18] using experimentally obtained equilibrium and profiles at the actual sensor positions. From the top, a combination of $n = 1$ and 2, $n = 1$ and $n = 2$ are shown as poloidal and toroidal patterns. Here, the ratio of the amplitudes of the $n = 1$ and $n = 2$ components and their phase difference are experimentally determined. The dotted lines again indicate mode pitch. The combination ($n = 1 + n = 2$) pattern closely reproduces the experimental signal pattern. In particular, the mode pattern pitches are almost identical. In this high-β plasma, it is found that $n = 1, 2$ and 3 ideal kink ballooning modes (IKBMs) are unstable without an ideal-wall (and stable with it) by MARS-F analyses. Thus, the $n = 1, 2$ and 3 IKBMs in this discharge can be said to be marginal modes even with an ideal-wall. Namely, these marginal modes can be driven by EPs at the same time. These EPdMs have been considered to be EP-driven IKBM or RWM branches

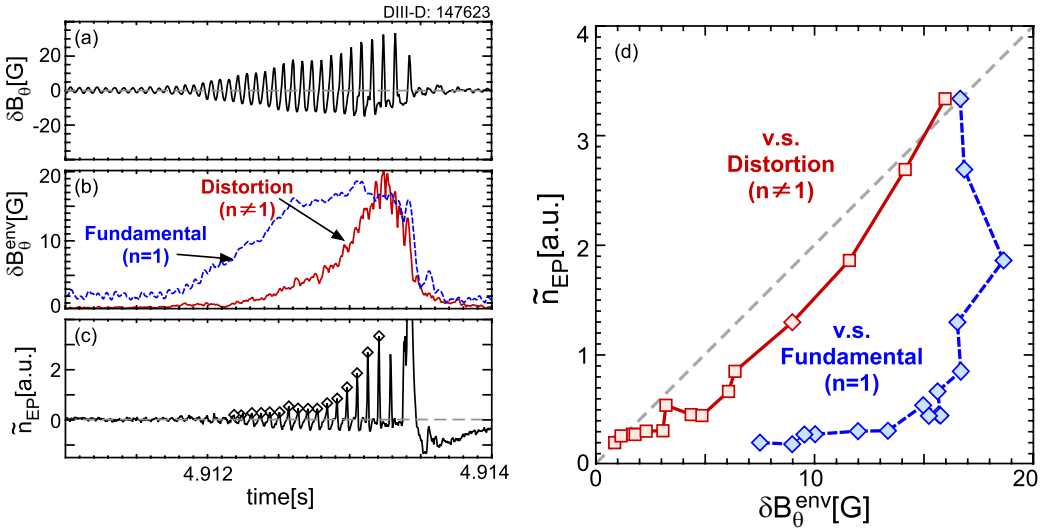

Figure 7. Dependence of EP density fluctuation versus fundamental ($n = 1$) and distortion ($n \neq 1$) components of EPdM on DIII-D. (a) Integrated Mirnov signal, (b) envelopes of decomposed fundamental and distortion components, (c) EP density fluctuation measured by the BES system at edge, and (d) EP density fluctuation versus fundamental and distortion components.

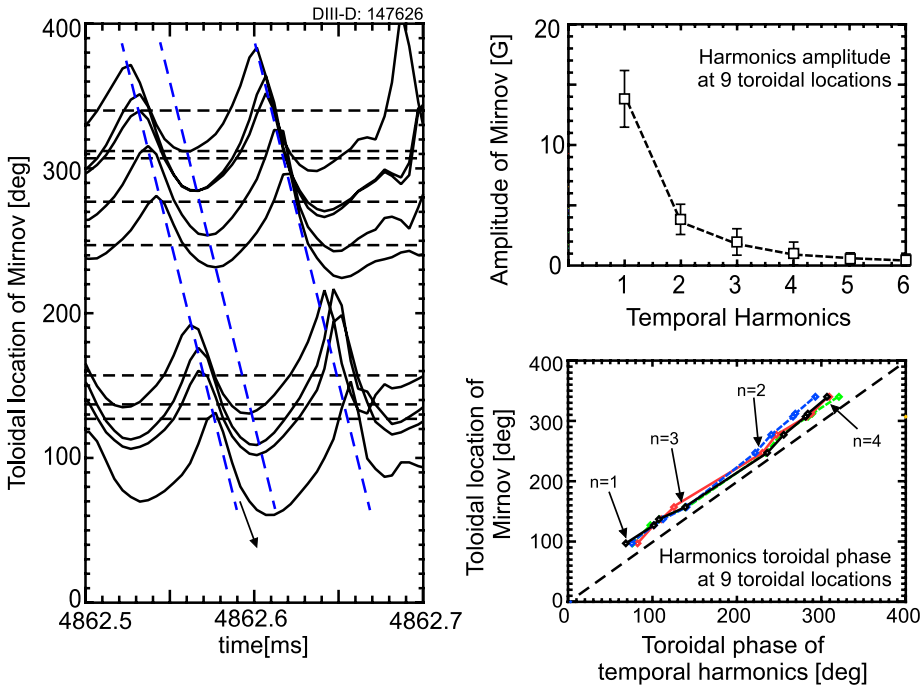

Figure 8. (a) Magnetic perturbations, (b) temporal harmonics amplitude and (c) phase relation between the fundamental and distortion portion observed by Mirnov probes located at nine different toroidal locations on the outboard side mid-plane.

because the observed EPdMs have a global mode structure similar to IKBM and RWM. Moreover, the maximum of the distortion component is always phase aligned with the maximum amplitude of fundamental component as indicated by the arrows in figures 10(b) and (c). Namely, the waveform distortion comes from branches other than $n = 1$, that are thought to be non-linearly destabilized in a synchronized manner with the $n = 1$ component.

Figures 11(a) and (b) are locations of Mirnov probes on the low field side on DIII-D and their integrated signals. A toroidally rotating helical structure of waveform distortion is observed. The waveform distortion is not only observed on the Mirnov signals but also in other measurements such as the electron density, electron temperature, and EP diagnostics [9]. Here, edge electron density in DIII-D measured by the CO_2 interferometeries are discussed. The perturbed edge density propagated as a wave packet like a 'density snake' since the distortion was highly localized in the toroidal direction. Figures 11(a) and (c) show the location of poloidal Mirnov probes on the low field side and the CO_2 interferometer chords. The CO_2 chord signals represent the line-integrated electron density. However, for the present H-mode-based experimental condition where a steep electron density gradient (∇n_e) dominates more at the edge than at the core, the observed

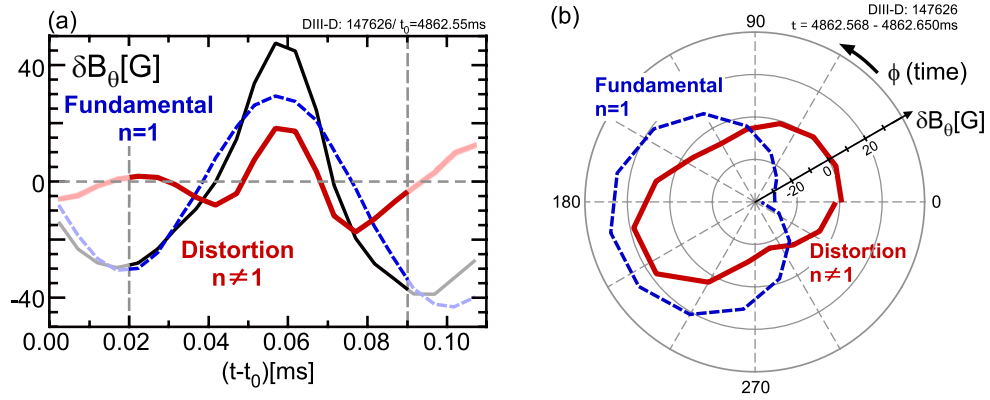

Figure 9. Phase relation between fundamental ($n = 1$) and distortion ($n \neq 1$) components. (a) One period of the EPdM waveform (solid), fundamental (dotted) and distortion (bold) components. (b) Polar plot of fundamental (dotted) and distortion (bold) components of the EPdM waveform on DIII-D. Azimuthal angle and radial direction correspond to toroidal angle and amplitudes of fundamental and distortion components.

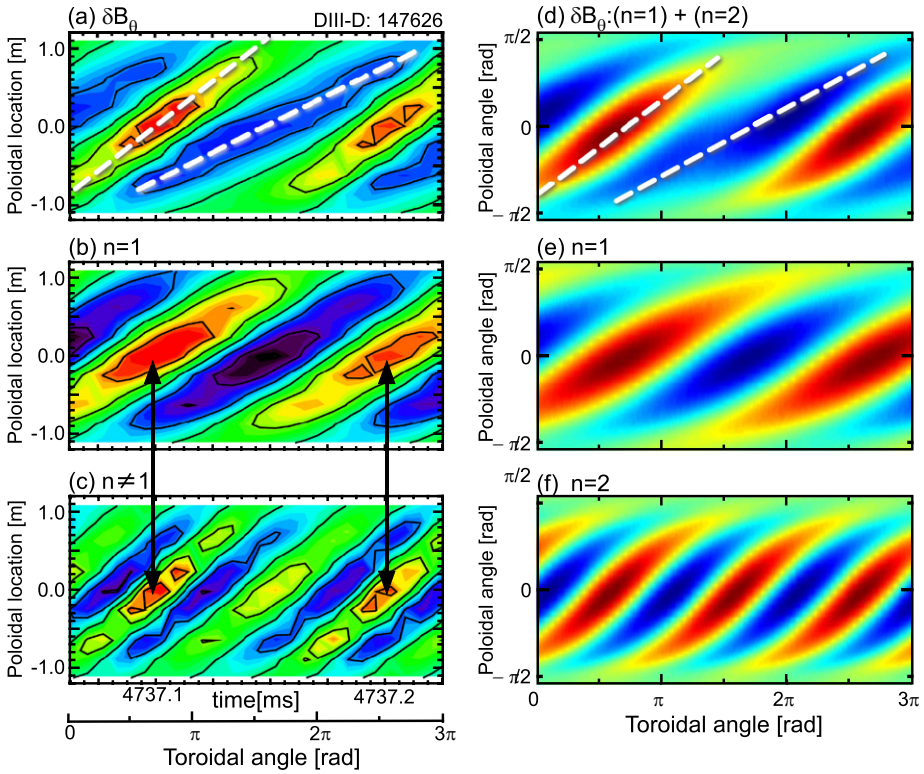

Figure 10. Experimentally obtained poloidal patterns of (a) integrated Mirnov signals δB_θ, (b) fundamental and (c) distortion components. Perturbation patterns of poloidal magnetic field by MARS-F: (d) combination of $n = 1$ and $n = 2$, (e) $n = 1$, and (f) $n = 2$ components.

fluctuations mainly come from the edge region. A helically-twisted density perturbation crosses twice through a given interferometry chord at the edge region: first at the top and later at the bottom. Observations show that a single snake structure produces two peaks in time, whose separation depends on the poloidal location of plasma edge for the individual chord as shown in figure 11(c). Figure 11(d) shows that waveform distortion has a filament-like snake helical structure only existing around LFS since the chord signal of V1 is weak compared with others. The fact that the poloidal pitch structure of magnetic fluctuation and edge density perturbation coincide well with each other as shown in figures 11(b) and (d) indicates that the EP transport and loss also ride on this helical structure.

3. Conditions of ELM triggering and pacing by EPdM

3.1. Conditions of ELM triggering by EPdM

ELM triggering by the EPdMs does not always occur. Since the waveform distortion strongly relates to the EP transport, the dependence of the waveform distortion on ELM triggering must be evaluated. Figure 12 shows ELM triggering dependence on fundamental and distortion amplitudes with (solid) and without (dotted) ELM triggering on (a) DIII-D and (b) JT-60U. The EPdM waveform is distorted when $\delta B_\theta^{n=1} \geqslant 10$ G. Diamonds in these diagrams correspond

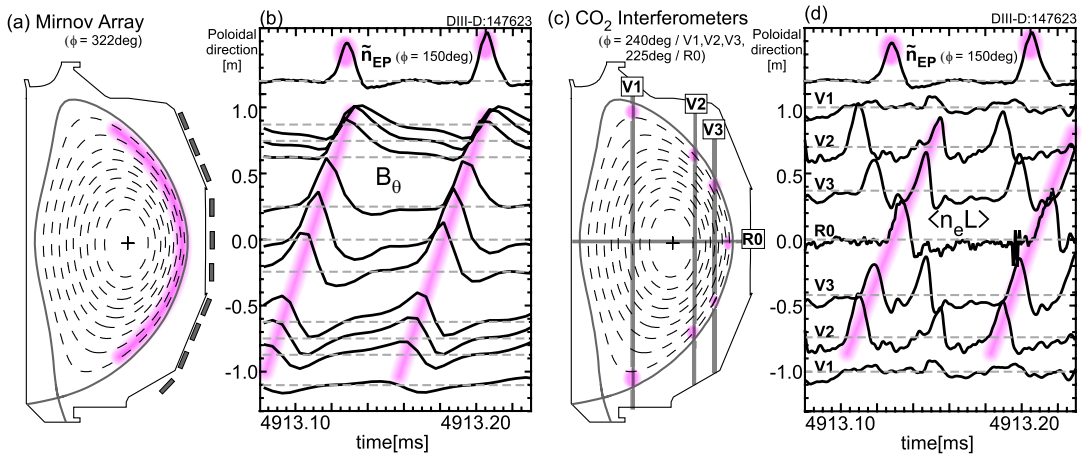

Figure 11. (*a*) EFIT equilibrium of 147626 at $t = 4.725$ s with Mirnov probe array at LFS on DIII-D and (*b*) integrated Mirnov signals versus time with EP density fluctuation measured by BES at the edge region. (*c*) EFIT equilibrium with CO_2 interferometer arrays (R0, V1, V2, V3) and (*d*) CO_2 interferometer signals versus time.

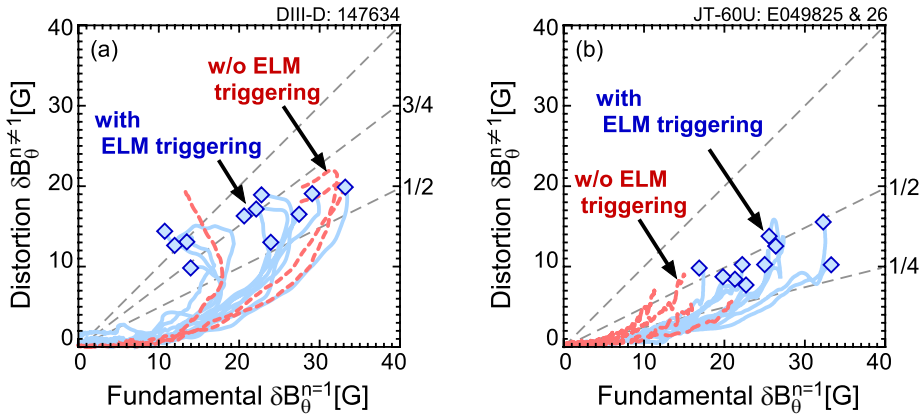

Figure 12. Amplitudes of fundamental ($n = 1$) and distortion ($n \neq 1$) components of EPdMs on DIII-D and JT-60U. Diamonds indicate ELM triggering. Dotted lines are cases without ELM triggering.

to ELM triggering times. ELM triggering seems to require a sufficient level of the waveform distortion (around three quarters or half of the fundamental component for DIII-D and JT-60U respectively). Note that the difference in these levels is thought to be due to the distance between the plasma and the Mirnov probe. Since this distance on JT-60U is a factor of 1.2 larger than that of DIII-D, the distortion component on JT-60U is thought to rapidly fall off toward the wall. However, no ELM triggering occurred in some cases even with large fundamental and distortion amplitudes as shown by the dotted lines. This means that the amplitude of the EPdM is a necessary condition, but not a sufficient one. In particular, an EPdM occurring immediately after the ELM crash cannot trigger an ELM.

Statistical analyses are performed to find other necessary conditions for ELM triggering by the EPdM. Namely, the EPdMs are categorized 'with' and 'without' ELM triggering. Figure 13 is a histogram of the EPdM maximum amplitude with (dotted) and without (solid) ELM triggering on DIII-D. In both cases, the probability histogram of EPdMs is broad with the peak at 30 G. In particular, ELM triggering requires an amplitude greater than 15 G. This leads to a conclusion that there is a threshold of the EPdM amplitude for ELM triggering.

Figure 14 shows a statistical analysis of the time delay of the EPdM from the last ELM crash Δt_{ELM} on DIII-D. The definition of Δt_{ELM} is also shown schematically in figure 14(*a*) 'with' and 'without' ELM triggering. Figure 14(*b*) shows histograms of Δt_{ELM} with and without ELM triggering. Note that the histogram of Δt_{ELM} shown in figure 14(*b*) is made by using only the data larger than 15 G amplitude shown in figure 13. Also, data with Δt_{ELM} less than 2.5 ms are removed because an ELM triggered by an EPdM or an accidental overlap between a natural ELM and an EPdM cannot be distinguished within the first few milliseconds of an ELM. As mentioned above, the average of the ELM repetition frequency is $f_{ELM} \simeq 200$ Hz, thus its period is $\tau_{ELM} \simeq 5$ ms. Namely, the pedestal recovery takes ~5 ms. The EPdM without ELM triggering has its at a shorter time than $\tau_{ELM} \simeq 5$ ms in contrast to those with ELM triggering. Meanwhile, the case with ELM triggering is a broad histogram. Namely, with the time delay shorter than the average ELM period, the pedestal condition is not fully recovered. In other words, the edge stability is not marginal. This is one possible cause that ELM triggering infrequently occurs just after the ELM crash in DIII-D. Namely, the pedestal recovery, thus marginal edge stability, is needed for ELM triggering by the EPdM. As a matter of fact, the EPdMs without ELM triggering shown in figure 12 have $\Delta t_{ELM} < 3.5$ ms on DIII-D. Therefore, ELM triggering by the EPdM needs the

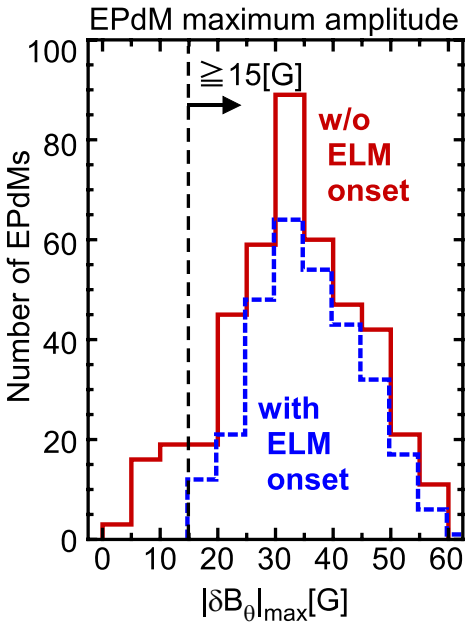

Figure 13. Statistical analysis of EPdM maximum amplitude $|\delta B_\theta|$ with and without ELM triggering on DIII-D.

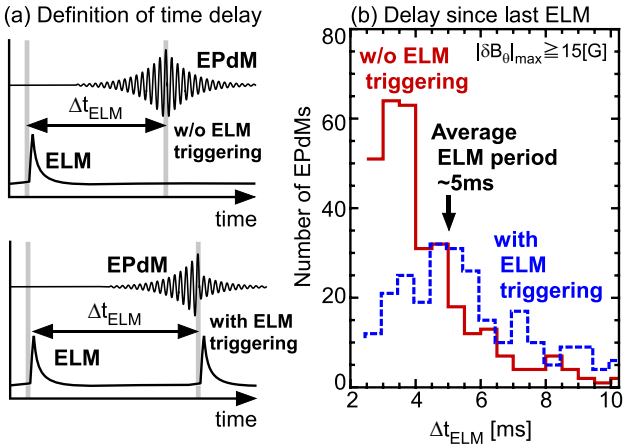

Figure 14. Statistical analysis of time delay from the last ELM with and without ELM triggering on DIII-D. (*a*) Definition of time delay Δt_{ELM} and (*b*) histograms of Δt_{ELM}.

marginal edge stability condition. Note that this case on DIII-D is not an ELM pacing case. ELM pacing is discussed next.

3.2. Conditions of ELM pacing by EPdM

Looking towards ITER, ELM control is an urgent issue to avoid large heat flux to the divertor and first wall. Therefore, large ELMs should be avoided or at least controlled. The observed ELM triggering by the EPdM in JT-60U indicates ELM mitigation like behaviour [4]. Here, the conditions for ELM pacing by the EPdM (that means ELMs fully synchronized with the EPdM bursts) are discussed.

ELM triggering by the EPdM looks different on DIII-D and JT-60U. Figure 15 shows typical waveforms of ELM triggering by the EPdM on (*a*) DIII-D and (*b*) JT-60U. On DIII-D, the EPdM and ELM are partially synchronized while on JT-60U, they are fully synchronized. Thus, the JT-60U case seems to pace ELM onset. To clarify what makes this difference between DIII-D and JT-60U, a database of repetition frequencies of the EPdM and ELM is made for a statistical analysis. Definitions of repetition frequencies are schematically shown in figure 16(*a*). Figures 16(*b*) and (*c*) are histograms of the EPdM and ELM repetition frequencies on DIII-D and JT-60U. These histograms are obtained from typical high-β_{N} discharges as shown in figure 1 (for 12 and 5 shots on DIII-D and JT-60U, respectively). On DIII-D, the natural ELM frequency f_{ELM} is about 200 Hz, that is twice as high as that of EPdM repetition frequency $f_{\mathrm{EPdM}} \simeq 100$ Hz. On JT-60U, the ELM has two repetition frequency peaks around 40 and 140 Hz. The peak at the lower frequency corresponds to the natural ELM frequency, and the peak at the higher frequency corresponds to the EPdM-paced ELM, thus $f_{\mathrm{ELM}} = f_{\mathrm{EPdM}}$. This looks like "ELM pacing" by the EPdM. Note that the relative height of the peaks in these histograms depends on the discharge pattern such as time duration with natural ELM phase and EPdM phase. Thus, the existence of two peaks is essential, that is, one corresponds to natural ELMs and the other corresponds to EPdM-paced ELM. From this, it is seen that frequent EPdM cycles can pace the ELM. Namely, when $f_{\mathrm{EPdM}} > f_{\mathrm{ELM}}$, which is the JT-60U case, ELM pacing by the EPdM can occur. However, if the period is too short ($f_{\mathrm{EPdM}} \gg f_{\mathrm{ELM}}$) not every EPdM can trigger an ELM due to the lack of pedestal recovery as explained above. Thus, an adequate balance between pedestal recovery and EP transport by the EPdM is needed.

4. Discussion for ELM triggering by EPdMs

4.1. Edge stability and possible mechanisms

Here, we discuss possible mechanisms of ELM triggering by the EPdM. Edge stability is usually discussed using the j–α diagram [19]. Namely, the edge stability is bounded by 'kink/peeling' and 'peeling–ballooning' modes destabilized by an edge current density j and pressure gradient α at the edge region. The α is a normalized pressure gradient ∇p defined as $\alpha \equiv -(\mu_0/2\pi^2)(\partial p/\partial\psi)(\partial V/\partial\psi)(V/2\pi^2 R)^{1/2}$, where μ_0 and V denote the permeability in the vacuum and the plasma volume in each flux surface ψ, respectively [20]. The edge stabilities in the high-β_{N} discharges on DIII-D and JT-60U are calculated by the linear MHD analysis codes ELITE [21] or MARG2D [22] respectively. Figures 17(*a*) and (*b*) correspond to calculated j–α diagrams for DIII-D and JT-60U. Experimental points just before ELMs are shown with crosses. The pedestal condition on DIII-D is close to the kink/peeling and peeling/ballooning stability boundaries. The condition on JT-60U is close to peeling–ballooning and ballooning stability boundaries. The difference between DIII-D and JT-60U is thought to be due to differences in the edge current densities [23].

Schematic j–α diagrams are shown in figure 18. Here, two possible mechanisms based on transported EPs by the EPdM are described. The first ELM triggering mechanism is the possibility of an additional pressure gradient of transported EPs caused by the EPdM. Transported EPs can act as an additional pressure δp_{EP} as shown in figure 18(*a*). It can increase the edge pressure gradient and violate the peeling–ballooning stability boundary. Since EPs have a large energy,

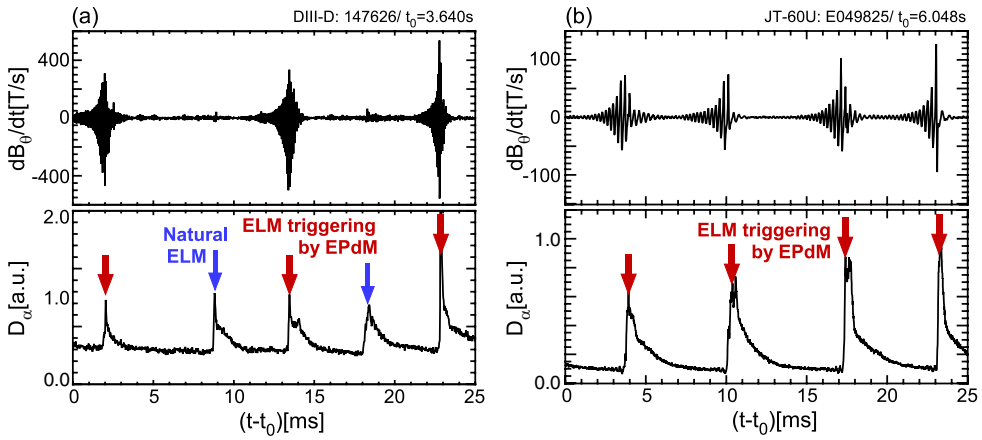

Figure 15. Comparison of synchronization between EPdMs and ELMs: (top) Mirnov signals and (bottom) D_α emissions on (*a*) DIII-D and (*b*) JT-60U.

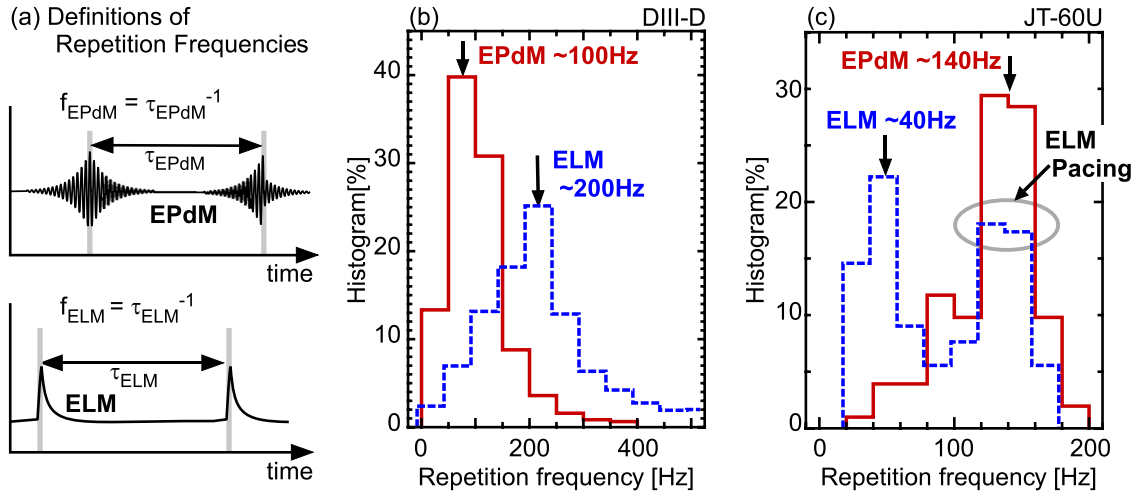

Figure 16. Statistical analysis of repetition frequencies of ELM and EPdMs. (*a*) Definition of repetition frequencies of EPdMs and ELMs. Histogram of repetition frequencies of EPdMs and ELMs on (*b*) DIII-D and (*c*) JT-60U.

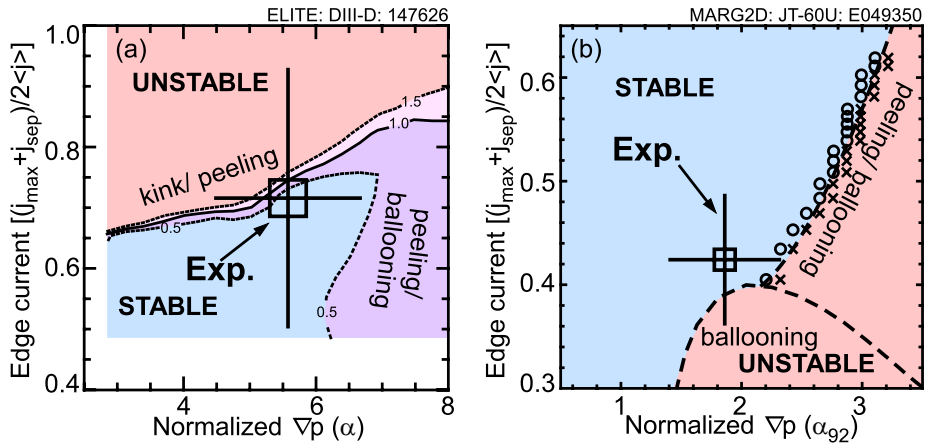

Figure 17. MHD stability at edge region. Numerical results of j-α diagrams on (*a*) DIII-D and (*b*) JT-60U calculated by ELITE and MARG2D, respectively.

transported EPs can affect edge stability even with a small increase in EP density. In this interpretation, not only $\nabla\delta p_{\mathrm{EP}}$ but also closeness to the stability boundary are critical to trigger the ELM. As shown in figure 17, increases in ∇p at the edge can reach to the peeling/ballooning stability boundary in both the DIII-D and JT-60U cases. If the impact of transported EPs by the EPdMs is sufficient to reach these stability boundaries, the ELM can be triggered. This is qualitatively consistent with the observation that ELM triggering infrequently occurred before a pedestal recovery, and consequently the EPdMs without ELM

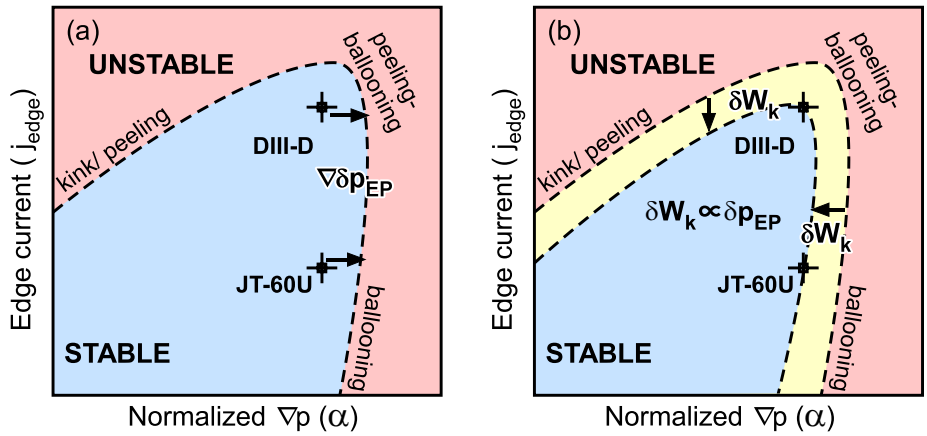

Figure 18. Possible mechanisms of ELM triggering by EPdMs. Schematic diagrams where (*a*) EP pressure affects as additional pressure and (*b*) EP kinetic contribution narrows stability boundary.

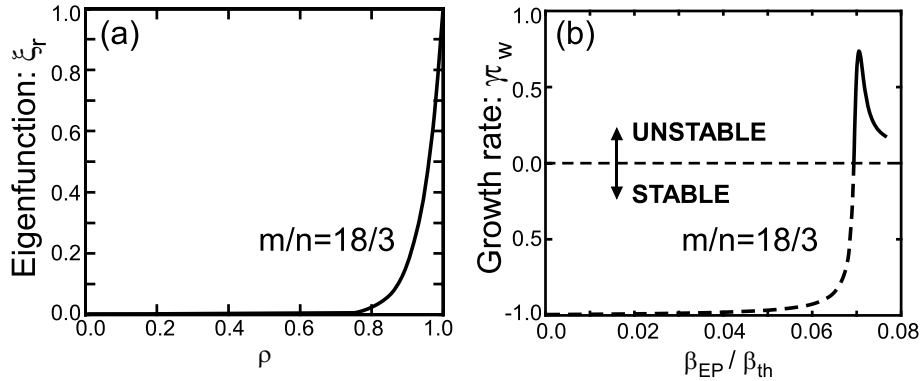

Figure 19. Analytical study of EP contribution to kink/peeling modes. (*a*) Eigenfunctions and (*b*) growth rates versus ratio between EP and thermal β of the 18/3 mode.

triggering occurred within a typical ELM period as shown in figure 14(*b*). A quantitative discussion is given in [4]. Namely, that the total stored energy of EPs around the $q = 2$ surface where the EPdM has a large amplitude is comparable to the local pedestal stored energy. This means that if a large enough EP energy is transported to the edge region by the EPdM, it could increase the pressure gradient and affect edge stability.

The second possibility is changing the stability boundary by an EP contribution. The transported EPs to the edge region where the stability is marginal can make a new EP branch. This EP branch is more unstable than usual the modes that can trigger the ELM. Thus, this EP contribution can narrow the stable region as shown in figure 18(*b*). As for the second possibility, the EP contribution to marginal edge stability is discussed below.

4.2. EP contribution to peeling mode

Here, a second possibility of ELM triggering by the EPdM is discussed. The transported EPs to the edge region where the stability is marginal due to the recovery of the pedestal top can make a new EP branch. To formulate this situation and then analytically investigate the EP contribution to the edge stability, the following simple dispersion relation with the resistive wall is used taking into account an EP kinetic effect [25]:

$$D(\omega) \equiv -\mathrm{i}\omega\tau_\mathrm{w} + \frac{\delta W_\mathrm{f}^\infty + \delta W_\mathrm{k}}{\delta W_\mathrm{f}^b + \delta W_\mathrm{k}} = 0,$$

where $\omega (= \omega_\mathrm{r} + \mathrm{i}\gamma)$ and τ_w are a complex mode frequency and a typical wall time constant of a resistive wall, and δW_f^b, $\delta W_\mathrm{f}^\infty$ and δW_k are bulk energies with and without the wall and the EP kinetic contribution. Drift-kinetic effects of EPs on the stability of the peeling mode are included using a formulation similar to the one developed for the RWM [26]. Note that the second possibility of ELM triggering by the EPdM corresponds to the non-adiabatic part of the integration of the drift-kinetic equation while the first one corresponds to the adiabatic part. Parameters assumed in this analysis are: minor and major radii $a = 1\,\mathrm{m}$ and $R = 3\,\mathrm{m}$ (the theory is developed in the large aspect ratio limit), toroidal magnetic field $B_\mathrm{t} = 2.3\,\mathrm{T}$, a cylindrical plasma with uniform safety factor slightly above an integer number $q = 6.02$, $\delta W_\mathrm{f}^\infty = 0.00123$, and $\delta W_\mathrm{f}^b = 0.00124$. A resistive wall is placed at the minor radius of $b = 1.05a$. In this approximation, the low-n ($n = 3$) peeling mode is considered with high poloidal mode number $m = 18$. Figure 19 shows eigenfunction magnitude and growth rate as a function of EP β-value β_EP. The eigenfunction ξ_r, that is the normal plasma displacement, scales roughly as r^{m-1}, representing a mode that progressively peaks near the plasma edge. Even though we still use the dispersion relation with the

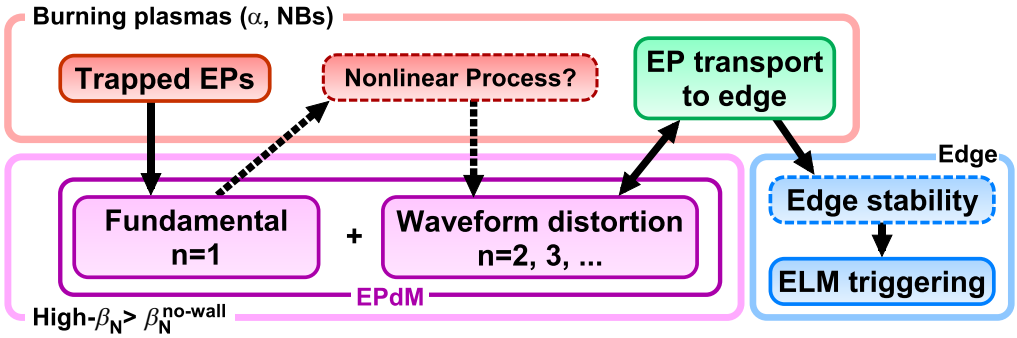

Figure 20. Summary diagram of ELM triggering by EPdMs. Solid lines and dotted lines are observed and conjectured physics, respectively.

resistive wall for this mode, the influence of the wall decreases as the modes become more peeling-like.

The peeling mode is potentially stable in the fluid approximation $\delta W_k \propto \beta_{EP} = 0$. By including EPs with a slowing down distribution in the particle energy space (the birth energy is assumed to be 85 keV) and a δ-function distribution in the particle pitch angle, $\delta(\lambda - \lambda_0)$, with $\lambda_0 = 1.43$, the stable peeling mode is destabilized with the increase of the EP pressure, where λ represents the pitch angle. The destabilization comes from the mode resonance with the toroidal precession of EPs. Thus, the destabilized mode is a new EP branch originated from a marginal low-n peeling mode the edge region. Note that the critical β_{EP} is sensitive to the value of the particle pitch angle, which can be found only in a certain region of the pitch angle λ_0. In this investigation, we found an unstable peeling mode when β_{EP} is of order of 0.1. More detailed discussion about the dependence of β_{EP} on λ_0 is presented in [25]. The critical β_{EP} to destabilize the peeling mode is also sensitive to the stability margin. This analytical investigation indicates that the stable ideal peeling mode with low-n and high-m can be triggered by EPs. Namely, the EP contribution can narrow the stable region compared with the usual modes that can trigger ELMs as shown in figure 18(*b*).

4.3. Possible interpretation for ELM triggering by EPdMs

Figure 20 is a diagram summarizing our interpretation of ELM triggering by EPdMs based both on the results and discussions. Here, solid and dotted lines are 'observed' and 'conjectured' physics, respectively. Namely, the interpretation is as follows:

- The EPdM is driven by trapped EPs,
- The waveform of the EPdMs is distorted, that may be non-linearly induced, as the fundamental component increases,
- The waveform distortion enhances EP transport to edge,
- The transported EPs affect edge stability, i.e., additional pressure gradient or EP contribution to marginal mode,
- Finally, ELM triggering occurs.

5. Summary

We have observed that the ELM can be triggered by the EP-driven modes in JT-60U and DIII-D. These observations imply that a common MHD physics in high-β plasmas exists. The interaction between the EPdM and ELM are reproducibly observed. Many EP diagnostics indicate a strong correlation between the distorted waveform of the EPdM required to trigger an ELM and the EP transport to edge. The waveform distortion is composed of higher harmonics, $n \geqslant 2$, and looks like a density snake near the plasma edge. The transported EPs are thought to affect edge stability. Moreover, ELM triggering by EPdMs infrequently occurs immediately after an ELM crash. This means that pedestal recovery, thus the marginal stability condition on the edge, is necessary for ELM triggering by the EPdMs. Based on these results, we discussed possible mechanisms of ELM triggering by the EPdM such as transported EPs by the EPdMs act as an additional pressure or change edge stability. Furthermore, it is found that ELM pacing occurs when the EPdM repetition frequency is higher than that of a natural ELM. These results indicate that EPs can become a major player even when edge stability is discussed for burning plasmas.

Acknowledgments

This work was supported in part by the US Department of Energy under DE-AC02-09CH11466, SC-G903402, DE-AC52-07NA27344, DE-FC02-04ER54698, DE-FG02-07ER54917, DE-AC04-94AL85000 and DE-FG02-08ER85195 and a Grant-in-Aid for Young Scientists (B) from the Ministry of Education, Culture, Sports, Science, and Technology of Japan, No 23760818. We are thankful to Drs E. Fredrickson, N. Ferraro and J. de Grassie for stimulus discussions on mode distortion.

References

[1] ITER Physics Basis 2007 *Nucl. Fusion* **47** S285
[2] Chu M.S. and Okabayashi M. 2010 *Plasma Phys. Control. Fusion* **52** 123001
[3] Matsunaga G. *et al* 2010 *Nucl. Fusion* **50** 084003
[4] Matsunaga G. *et al* 2013 *Nucl. Fusion* **53** 073046
[5] Matsunaga G. *et al* 2009 *Phys. Rev. Lett.* **103** 045001
[6] Okabayashi M. *et al* 2009 *Nucl. Fusion* **49** 125003
[7] Okabayashi M. *et al* 2011 *Phys. Plasmas* **18** 056112
[8] Murakami M. *et al* 2009 *Nucl. Fusion* **49** 065031
[9] Heidbrink W.W. *et al* 2011 *Plasma Phys. Control. Fusion* **53** 085028
[10] Heidbrink W.W. *et al* 1986 *Rev. Sci. Instrum.* **57** 1769
[11] Fisher R.K. *et al* 2010 *Rev. Sci. Instrum.* **81** 1769
[12] Heidbrink W.W. *et al* 2011 *Plasma Phys. Control. Fusion* **53** 085007
[13] Muscatello C.M. *et al* 2010 *Rev. Sci. Instrum.* **81** 10D316
[14] Zhu Y. *et al* 2012 *Rev. Sci. Instrum.* **83** 10D304

[15] White R. *et al* 1983 *Phys. Fluids* **26** 2958
[16] Chen X. *et al* 2012 *Rev. Sci. Instrum.* **83** 10D707
[17] Park W. *et al* 1995 *Phys. Rev. Lett.* **75** 1763
[18] Liu Y. *et al* 2010 *Plasma Phys. Control. Fusion* **52** 104002
[19] Wilson H.R. *et al* 2006 *Plasma Phys. Control. Fusion* **48** A71–84
[20] Pankin A.Y. *et al* 2005 *Plasma Phys. Control Fusion* **47** 483
[21] Wilson H.R. *et al* 2002 *Phys. Plasmas* **9** 1277
[22] Aiba N. *et al* 2006 *Comput. Phys. Commun.* **175** 269–89
[23] Oyama N. *et al* 2008 *J. Phys: Conf. Ser.* **123** 012002
[24] Liu Y. *et al* 2010 *Nucl. Fusion* **50** 095008
[25] Hao G.Z. *et al* 2013 *Phys. Plasmas* **20** 062502
[26] Hao G.Z. *et al* 2011 *Phys. Rev. Lett.* **107** 015001